Fermilab FERMILAB-Pub-01/045-E CDF July 2001

CDF/PUB/PLUG_UPGR/PUBLIC/5545
Final NIM draft, Version 1.4 (March 6, 2001)

The CDF Plug Upgrade electromagnetic calorimeter: test beam results

M. Albrow[a], S. Aota[b], G. Apollinari[c], T. Asakawa[b], M. Bailey[d], P. de Barbaro[e], V. Barnes[f], K. Biery[a], A. Bodek[e], L. Breccia[g], R. Brunetti[g], H. Budd[e], D. Cauz[h], L. Demortier[c], I. Fiori[g], M. Frautschi[i], Y. Fukui[j], O. Ganel[i,1], Y. Gotra[k,2], S. Hahn[a], T. Handa[l], K. Hatakeyama[m,3], H. Ikeda[b], G. Introzzi[n], J. Iwai[m], T. Kikuchi[b], S.H. Kim[b], W. Kowald[o], A. Laasanen[f], J. Lamoureux[p], M. Lindgren[q], J. Liu[e], S. Lusin[r], P. Melese[c,4], H. Minato[b], S. Murgia[s], H. Nakada[b], J. Patrick[a], G. Pauletta[h], W. Sakumoto[e], L. Santi[h], Y. Seiya[b], A. Solodsky[c], R. Wigmans[i], S. Zucchelli[g]

[a] *Fermi National Accelerator Laboratory, Batavia, IL 60510, USA*
[b] *University of Tsukuba, Tsukuba, Ibaraki 305, Japan*
[c] *Rockefeller University, New York, NY 10021, USA*
[d] *University of New Mexico, Albuquerque, NM 87131, USA*
[e] *University of Rochester, Rochester, NY 14627, USA*
[f] *Purdue University, West Lafayette, IN 47907, USA*
[g] *Istituto Nazionale di Fisica Nucleare, University of Bologna, I-40126 Bologna, Italy*
[h] *Universita di Udine e Sezione INFN di Trieste, I-33100 Udine, Italy*
[i] *Texas Tech University, Lubbock, TX 79409, USA*
[j] *High Energy Accelerator Research Organization (KEK), Tsukuba, Ibaraki 305, Japan*
[k] *Universita di Padova, Instituto Nazionale di Fisica Nucleare, Sezione di Padova, I-35131 Padova, Italy*
[l] *Hiroshima University, Higashi-Hiroshima, Hiroshima 739, Japan*
[m] *Waseda University, Shinjuku, Tokyo 169, Japan*
[n] *Universita e Sezione INFN di Pavia, I-27100 Pavia, Italy*
[o] *Duke University, Durham, NC 27708, USA*
[p] *Brandeis University, Waltham, MA 02254, USA*
[q] *University of California at Los Angeles, Los Angeles, CA 90024, USA*
[r] *University of Wisconsin, Madison, WI 53706, USA*
[s] *Michigan State University, East Lansing, MI 48824, USA*

Abstract

The CDF Plug Upgrade calorimeter, which fully exploits the tile-fiber technique, was tested at the Fermilab meson beamline. The calorimeter was exposed to positron, positively charged pion and positive muon beams with energies in the range of 5–230 GeV. The energy resolution of the electromagnetic calorimeter to the positron beam is consistent with the design value of $16\%/\sqrt{E} \oplus 1\%$, where E is the energy in units of GeV and $\oplus$ represents sum in quadrature. The non-linearity for positrons is studied in an energy range of 11–181 GeV. It is important to incorporate the response of the preshower detector, the first layer of the electromagnetic calorimeter which is read out separately, into that of

[1]Present address: IPST University of Maryland at College Park, College Park, Maryland 20742.
[2]Present address: University of Pittsburgh, Pittsburgh, Pennsylvania 15260.
[3]Present address: Rockefeller University, New York, New York 10021.
[4]Present address: SRI International, Menlo Park, California 94025-3493.

the calorimeter to reduce the non-linearity to 1% or less. The energy scale is about 1.46 pC/GeV with HAMAMATSU R4125 operated typically at a gain of 2.5×10^4. The response non-uniformity over the surface of a tower of the electromagnetic calorimeter is found to be about 2% with 57 GeV positrons. Studies of several detailed detector characteristics are also presented.

1 Introduction

The CDF Plug Upgrade calorimeter [1, 2] is a shower-sampling device consisting of plastic scintillating plates with optical fiber readout. This device replaces the previous gas sampling calorimeters in the CDF Plug and Forward/Backward regions in order to cope with a bunch spacing as short as 132 ns in Tevatron Run-II collider runs. It represents the first application of the tile-fiber technique [3, 4] on a large scale. Besides faster responses of the calorimeter, its performance is expected to be as good as the CDF Central calorimeter [5, 6, 7]. The R&D results of the tile-fiber system for the CDF Plug electromagnetic calorimeter (PEM) are found in [8, 9]. Details of mass production and quality control are described in [10, 11, 12].

Beam tests were carried out for a beam test module of the CDF Plug Upgrade calorimeter at the Fermilab Meson-Test beamline from December 1996 to September 1997. We describe results for the PEM in this article. Those for the Plug hadronic calorimeter (PHA) are presented separately in this journal.

2 Setup

2.1 Test module

The beam test module is a replica of the real detector, spanning 45° and 60° in the azimuthal angle ϕ for the PEM and PHA, respectively. Figure 1 shows a cross section of the calorimeter. Briefly, the PEM is comprised of 22 sets of alternating layers of absorber and polystyrene scintillator covering a pseudorapidity ($\eta = -\ln\tan(\theta/2)$) region of $1.10 \leq |\eta| \leq 3.64$. The absorber plates are 4.5 mm thick lead sheets, on both sides of which 0.5 mm thick stainless-steel sheets are glued to reinforce mechanical rigidity and to weld them to structural supports. The scintillator thickness is 4 mm. Each scintillating layer is separated into 24 (12) mechanically independent sub-assemblies in ϕ for the PEM (PHA). In each sub-assembly, the scintillating plate is segmented into pieces (tiles) to form a projective tower geometry as the whole of the calorimeter system. There are 20 towers in each 15°-section, or wedge, as shown in Fig. 2. As a result of the projective tower geometry and the cylindrical shape of the PEM, the outermost two towers in a wedge consist of only the first fourteen layers. A wavelength-shifting (WLS) fiber (0.83 mm diameter) is embedded along a circular, so-called σ-shape, groove in each tile for readout. An exception is the innermost (smallest) tiles which have a S-shaped fiber routing due to geometrical difficulty. The light yield of these tiles is typically one half of the standard one [12]. The WLS fiber is spliced [13] to a clear fiber (0.83 mm diameter) just after exiting the tile and led to an optical mass-connector housing 10 fibers [14]. We connect flat cables of 10 clear fibers (0.9 mm diameter and $\simeq$ 3 m long) to the calorimeter end to transmit light to decoder

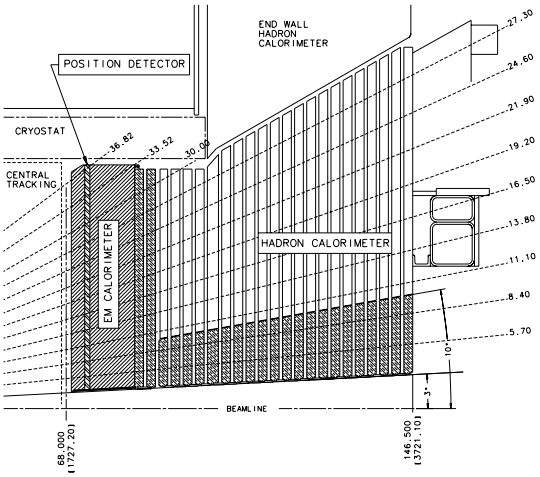

Figure 1: Cross section of an upper part of the CDF Plug Upgrade calorimeter.

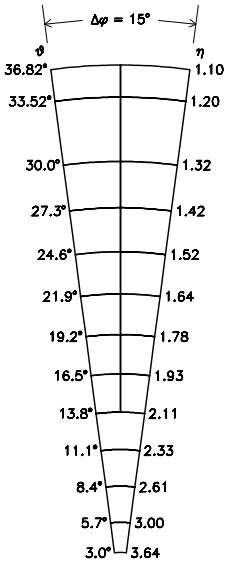

Figure 2: Tower segmentation of the CDF Plug Upgrade calorimeter.

boxes which consist of clear fibers (1.0 mm diameter and $\simeq$ 1 m long) to rearrange the signals into a tower-wise organization. The calorimeter is located inside a 1.4 T superconducting solenoid in actual operation, and the use of flexible clear fibers with long attenuation length ($\simeq$ 7.3 m) allows photon readout in a region free from the solenoidal magnetic field.

Just behind the 4th lead plate, the PEM also incorporates a shower-max position detector (PES) composed of plastic scintillator strips (5 mm wide and 6 mm thick) with optical fiber readout [15]. A basic mechanical unit spans 45° in ϕ and has two layers of strips with a 45° crossing angle.

In front of the first lead plate is another scintillator layer, which is read out separately from the rest of the calorimeter, to act as a preshower detector (PPR). Its structure is the same as the EM layers, except that the scintillator thickness is 10 mm and the fiber grooves are deeper, accepting two-turns of the WLS fiber. The tile segmentation matches the calorimeter tower geometry. The PPR is physically contained in the PEM structure and a structural cover plate made of 1.27 cm thick stainless-steel serves as a radiator. The beam test results for the PPR are presented in [16].

The PHA covering $1.3 \leq |\eta| \leq 3.64$ has a structure similar to the PEM but the thickness of the scintillator is 6 mm and the absorber is 5.08 cm thick iron.

We use photomultiplier tubes for photon readout. The PEM and PHA are read out by HAMAMATSU R4125, while the PES and PPR are read out by 16-channel multianode phototubes, HAMAMATSU R5900-M16. Typical light yields are 6, 6, and 10 photoelectrons per minimum ionizing particle (MIP) per tile for the PEM, PHA, and PPR, respectively, and 2 photoelectrons per MIP per bar for the PES.

All photomultiplier tubes were powered by CAEN SY527 high voltage power supplies. The SY527 is a crate-based high voltage system, able to accomodate up to ten different types of cards simultaneously. The high voltage generator card used in our system was the A932AN. This unit includes an internal high voltage generator that fans out the voltage to 24 distributed output channels. The generator (primary channel) can provide up to a maximum of 13 mA at 2500 V. Each distributed channel voltage can be independently regulated in a range of 900 V below the input voltage provided by the primary channel.

Table 1 summarizes the basic parameters of the calorimeter, together with those of the preshower detector and the shower-max position detector.

The test module was put on a computer-controlled table so that the beam incidence along the η direction became the same as in the actual collision hall, accounting for the $\cos^{-1}\theta$ effect in shower sampling. We also placed an aluminum plate of 3.81 cm ($0.43X_0$) thickness in front of the calorimeter to simulate the end plate of the central tracking detector. The total material in the beamline due to air, chamber vessels, etc. is estimated to be $0.36X_0$ [17]. The phototube gains were set to $\simeq 2.5 \times 10^4$ and $\simeq 2.5 \times 10^5$ for the PEM and PHA, respectively. The wedge and tower numbering conventions are given in Fig. 3. The definition of the coordinates is also shown in the figure.[1]

[1]The definition of the ϕ direction follows the one in the real operation, while the x and y directions are defined according to the beamline convention. This is why the two coordinate systems do not match.

Table 1: Parameters of the CDF Plug Upgrade preshower detector, the calorimeter, and the shower-max position detector.

	Plug PreRadiator (PPR)	
Type	tile-fiber ($\simeq 10 \times 10$ cm^2)	
Scintillator	10 mm polyvinyltoluene (BC408)	
WLS fiber	Y11, 200 ppm, 0.83 mm ϕ, multiclad, S type	
Preradiator	Steel plate (1.27 cm) of the PEM structure	
Depth	$\simeq 1.9\ X_0$ from the interaction point	
Phototube	HAMAMATSU R5900-M16 (multianode, 16 channels)	
Photoelectrons/MIP/tile	$\simeq 10$	
	Plug ElectroMagnetic (PEM)	Plug HAdron (PHA)
Type	tile-fiber ($\simeq 10 \times 10$ cm^2)	tile-fiber ($\simeq 20 \times 20$ cm^2)
Scintillator	4 mm polystyrene (SCSN38)	6 mm polystyrene (SCSN38)
WLS fiber	Y11, 0.83 mm ϕ, multiclad	
	200 ppm, S type	250 ppm, non-S type
Absorber	4.5 mm lead	5.08 cm iron
Layers	22	22
Thickness	36 cm ($20.1X_0$, $1.0\lambda_I$)	160 cm ($7.1\lambda_I$)
Depth segments	1	1
Phototube	HAMAMATSU R4125	
Photoelectrons/MIP/tile	$\simeq 6$	$\simeq 6$
	Plug Electromagnetic Shower-max (PES)	
Type	bar-fiber (strip size: 5 mm wide)	
Scintillator	6 mm polyvinyltoluene (BC408)	
WLS fiber	Y11, 350 ppm, 0.83 mm ϕ, multiclad, non-S type	
Depth	$\simeq 5.4\ X_0$ from the interaction point	
Layers	u-v, 45° crossing angle	
Phototube	HAMAMATSU R5900-M16 (multianode, 16 channels)	
Photoelectrons/MIP/bar	$\simeq 2$	

2.2 Momentum tagging and trigger system

Figure 4 shows the experimental setup of the beam test. The calorimeter was exposed to positrons, positive pions, and positive muons[2] in the energy range of 5–230 GeV.

Momentum tagging was provided by a set of bending magnets located between two pairs of single wire drift chambers (SWDCs). The momentum resolution is 1.8% at 5 GeV/c and improving with increasing momentum to 1.1% at 150 GeV/c. The contributions to the momentum uncertainty are the magnetic field strength and its detailed structure inside the dipole magnets. For momenta greater than 150 GeV/c, the resolution is 1.6%, as a result of an additional uncertainty caused by the saturation of the magnets. A typical beam-momentum distribution and beam profiles are shown in Fig. 5 for the electron beam, with the nominal momentum 50 GeV/c. Stabilities (reproducibilities) of the average and the rms values of the beam momentum are both better than 1% for all the available energies. The beam profiles in terms of the average position and the rms are also stable to better than 2 mm. Table 2 shows average beam momenta and rms values from typical data-taking runs for the beam tunes used in our analysis.

The electron trigger was made of 4-fold coincidence of beam trigger counters with vetoes on beam halo and delayed particles. The purity of the electron beam is estimated to be greater than 99%. The pion trigger was formed by adding, as a veto, a preshower counter with a $5.6X_0$ thick lead plate (TPSD) to the electron trigger logic to remove residual electrons in the pion beam. The electron contamination is negligible for energies greater than 7.5 GeV. For the muon beam with energies above 50 GeV, we added a 2-fold set of trigger counters to the electron trigger. The counters were located downstream of the calorimeter and after an additional $8\lambda_I$ of iron absorber. For muon beams with energies lower than 50 GeV, we further added a large trigger counter located between the calorimeter and the iron absorber to catch muons multiply-scattered through the calorimeter.

2.3 Front-end electronics

We employed the custom-designed RABBIT [18] system as the front-end readout electronics, which had been used at CDF in the previous collider runs. This crate-based system houses various front-end modules such as ADCs and TDCs, and its operation and readout are controlled by dedicated remote processors. Charge integration and signal amplification were performed by the PhotoMultiplier Amplifier (PMA) cards [18]. The sensitivity of the ADC is 11.4 fC/count with a full scale of 750 pC. It was operated with an ADC gate width of 2.2 μs. The typical rms of noise charge is $\simeq$ 40 fC.

2.4 Source and laser calibration

A motor-driven wire-source [19, 20] and laser calibrations [21] have been adopted at CDF as basic calibration methods during the course of Run-II. For the wire-source calibration, stainless steel tubes are attached to the cover plates of the scintillating tiles. They run down the middle of

[2]In the text, electrons, pions, and muons refer to positively charged particles of these species unless specifically noted otherwise.

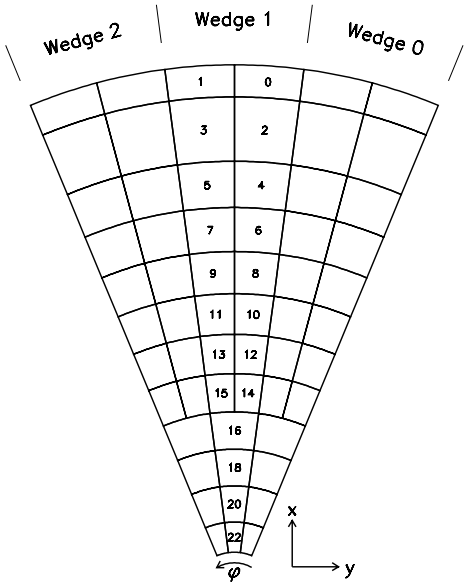

Figure 3: Wedge and tower numbering schemes, together with the coordinate definition. Refer to the text on the mismatch between the ϕ direction and the x-y system.

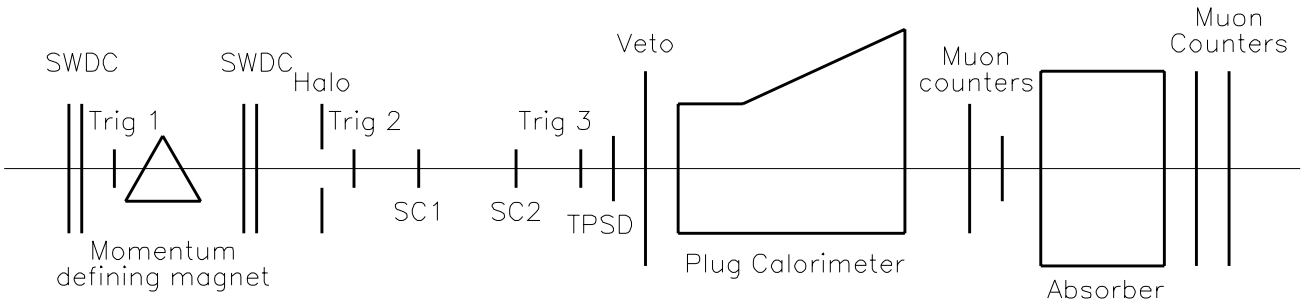

Figure 4: Setup of the beam test for the CDF Plug Upgrade calorimeter.

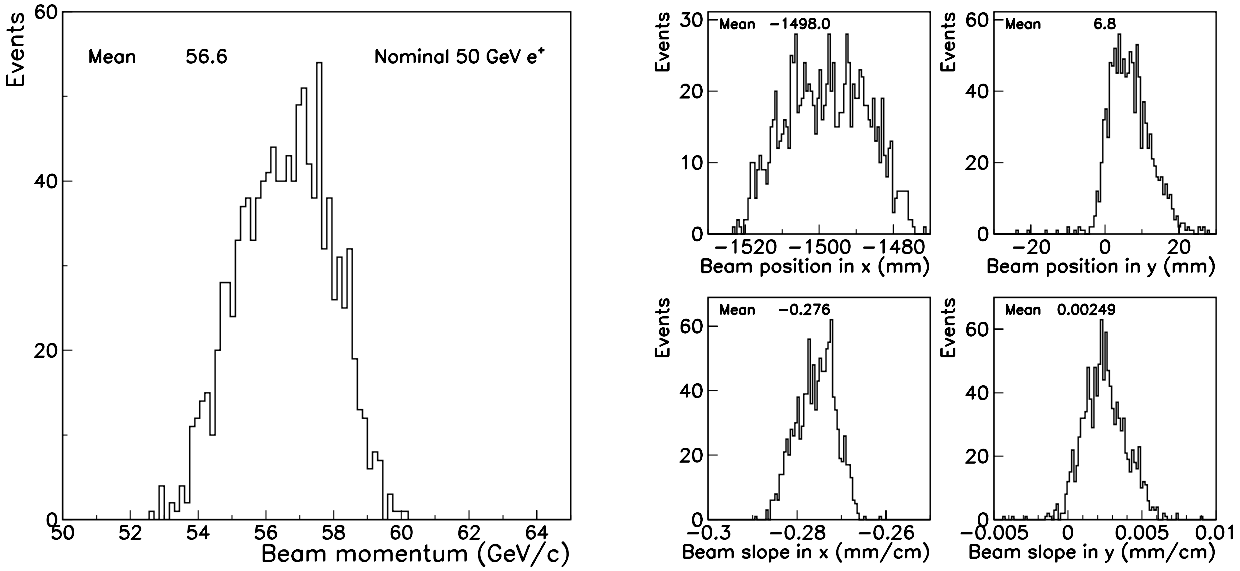

Figure 5: Typical distribution of measured beam momentum and beam profiles for the electron beam with the nominal momentum 50 GeV/c. The beam position shown is at the PEM detector surface.

Table 2: Typical measured momenta for various beam tunes.

	Electron		Pion		Muon	
Nominal (GeV/c)	Average (GeV/c)	rms (%)	Average (GeV/c)	rms (%)	Average (GeV/c)	rms (%)
5	5.34	2.1	—	—	—	—
7.5	9.07	2.1	8.64	2.3	—	—
10	11.4	2.0	12.2	1.6	11.9	3.2
25	28.2	2.4	28.7	0.9	28.4	2.5
50	56.5	2.4	57.9	0.9	57.6	2.2
75	91.0	2.4	90.3	0.7	90.2	4.1
100	122.	2.6	—	—	120.	3.3
125	150.	2.4	—	—	—	—
150	181.	2.5	171.	0.7	180.	2.8
227	—	—	231.	0.8	—	—

each tile, and ^{60}Co wire sources move through these tubes to irradiate each tile in each layer. The wire sourcing provides a gain calibration for the entire optical system including the scintillating tile, the WLS fiber, the clear fiber, and the phototube. In addition to the wire-source calibration, we have a laser calibration system to monitor phototube gains separately. This system sends laser light into each phototube. Pin-diodes are used to monitor the pulse-to-pulse variation in the laser-light intensity.

These calibration systems were installed in the beam tests as well.[3] The primary use of the wire sourcing in the beam tests was, however, to transfer energy scales determined for the beam test module to the real calorimeter system and to estimate its accuracy, rather than actual monitoring and calibration of the beam test module.

3 Results

3.1 Pedestal subtraction

By implementing randomly generated triggers between beam particles, we monitored the ADC pedestal shifts during the beam spill. The average pedestal count of each channel is calculated by fitting a Gaussian function to the ADC count distribution obtained by selecting the pedestal triggers. This pedestal count estimation is performed on a run-by-run basis, where a single run was usually taken with a fixed beam energy and a fixed calorimeter position with respect to the beamline. The average pedestal shifts in a run are typically a few counts and the fitted Gaussian sigmas (fluctuation in a run) are about 4 counts.

We check the systematics of the pedestal count estimation by looking at towers far from the beam and comparing responses collected with the pedestal and the beam triggers. We observe small differences which seem to be common to the PPR, PEM, and PHA, and thus could be attributed to a grounding instability of the electrical readout devices. Averaging over many towers, pedestal counts based on the pedestal trigger turn out to be larger than those from the beam trigger by 0.3–0.7 counts depending on the beam type and the beam energy. These systematic differences are, however, only important in the shower leakage study discussed in Section 3.9. The spread of the shifts over the towers is about 1 count which we quote as the uncertainty of the pedestal estimation.

3.2 Tower-to-tower response non-uniformity

Since the phototube gains were all set to $\simeq 2.5 \times 10^4$, any differences in the tower responses reflect differences of the light yields of the optical systems and the quantum efficiencies of the phototubes. This response non-uniformity is estimated by using data of 57 GeV electrons in the center of each tower. We define the calorimeter response to electrons as a 3×3 tower sum around the tower with beam:

$$E_i^{\rm EM} \equiv \sum_j^{3\times 3} E_j \frac{r_i^{\rm EM}}{r_j^{\rm EM}},$$

[3] We used ^{137}Cs as the wire source instead of ^{60}Co.

where i is the index of the tower with beam, E_j is the jth tower response, and $r_i^{\rm EM}$ is the relative response correction factor for the ith tower. The notation for the clustering window, "3×3", is actually symbolic, since we use a special window for tower 16 as shown in Fig. 6. Note that $E_i^{\rm EM}$ is only corrected for the tower-to-tower non-uniformity of adjacent towers with respect to the central tower (the ith tower) as a result of the inserted factor $r_i^{\rm EM}$. This is merely due to a technical reason that we would like to determine $r_i^{\rm EM}$ by iteration. The fully corrected response is given by $E_i^{\rm EM}/r_i^{\rm EM}$.

We choose tower 8 in wedge 1 (W1T08) as the reference tower to define $r_i^{\rm EM}$:

$$r_i^{\rm EM} \equiv \frac{\left\langle E_i^{\rm EM}/p \right\rangle}{\langle E_0^{\rm EM}/p \rangle}, \qquad E_0^{\rm EM} \equiv E_{\rm W1T08}^{\rm EM},$$

where p is the measured momentum and the average value $\langle E/p \rangle$ is calculated by fitting a Gaussian function. We obtain $r_i^{\rm EM}$ by iterating the calculation starting from $r_1^{\rm EM} = r_2^{\rm EM} = \cdots = 1$. The values become stable to a 0.5% level after a couple of iterations. Figure 7 shows the correction factors.[4] The mean value is 0.999 which is essentially the same as the reference tower. A typical distribution of the PEM response is shown in Fig. 8.

In a similar way, we obtain tower-to-tower (or, more precisely, tile-to-tile) response correction factors for the PPR, $r_i^{\rm PR}$. Since the PPR response is not as correlated with the electron momentum as the PEM response, we do not normalize the PPR response to the measured momentum but simply use the average value in the range of 0–3500 counts. Figure 9 shows the correction factors for the PPR. The large non-uniformity is mostly due to the gain variation between the channels in a multianode phototube. An example of the PPR response is shown in Fig. 10.

3.3 Total EM response

We calculate the total EM response to an electron as a weighted sum of the PEM and PPR responses:

$$E_i[\text{GeV}] = C' \left(E_i^{\rm EM}[\text{GeV}] + w \cdot E_i^{\rm PR}[\text{GeV}] \right),$$

where E_i is the calibrated energy for the ith tower, C' is the scale factor, $E_i^{\rm EM}$ and $E_i^{\rm PR}$ are the energies deposited in the PEM and PPR scintillators, respectively, and w is the preshower weight factor. We can rewrite this equation with observable quantities:

$$E_i[\text{GeV}] = C[\text{GeV/ADC}] \left(\frac{E_i^{\rm EM}[\text{ADC}]}{\tilde{r}_i^{\rm EM}} + w \cdot \frac{\alpha_0^{\rm EM}[\text{ADC/GeV}]}{\alpha_0^{\rm PR}[\text{ADC/GeV}]} \cdot \frac{E_i^{\rm PR}[\text{ADC}]}{\tilde{r}_i^{\rm PR}} \right), \qquad (1)$$

where $\tilde{r}_i$ is the relative response with respect to the reference tower, and α_0 is the conversion factor from GeV to ADC counts for the reference tower. For simplicity, we replace $\tilde{r}_i$ with the r_i obtained in the previous section: $\tilde{r}_i = r_i$. The ratio $\alpha_0^{\rm EM}/\alpha_0^{\rm PR}$ is estimated by looking at responses to 180 GeV muons which are shown in Fig. 11. The solid lines in the figure are fitting results from a Landau-Poisson-Gaussian convolution function. Taking into account the thickness difference between the PEM tower and PPR tile, we obtain $\alpha_0^{\rm EM}/\alpha_0^{\rm PR} = 0.118$.

[4] Error bars shown in the figures and quoted uncertainties in the text are statistical unless noted otherwise.

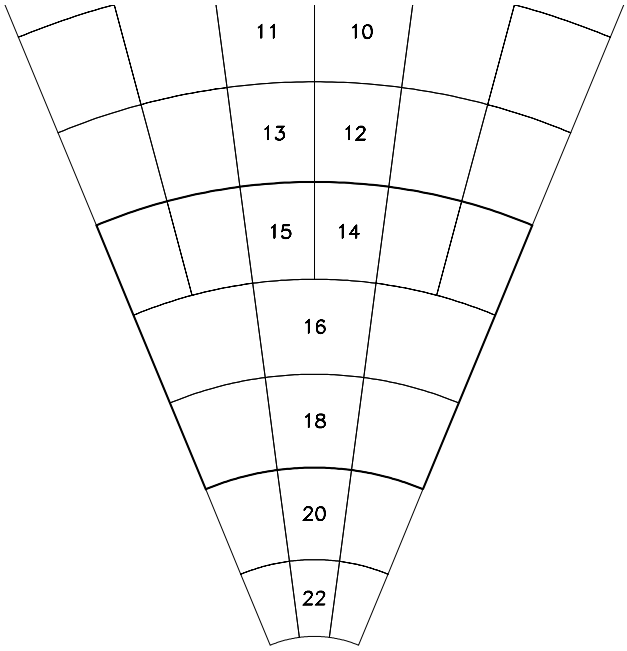

Figure 6: Clustering window used in our analysis for tower 16.

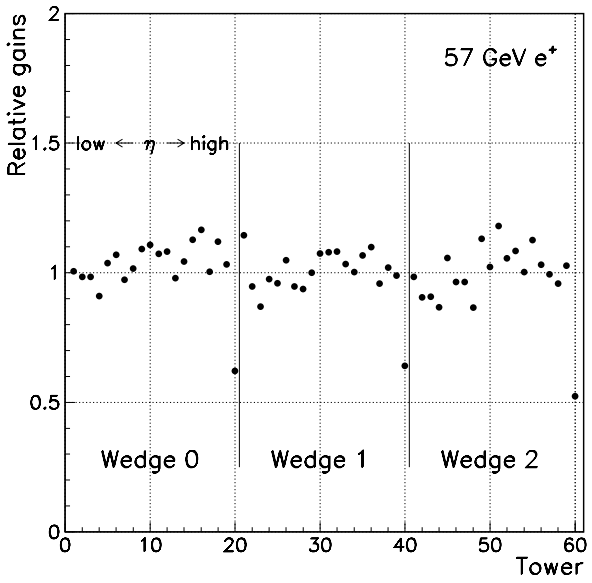

Figure 7: Tower-to-tower response non-uniformity of the PEM.

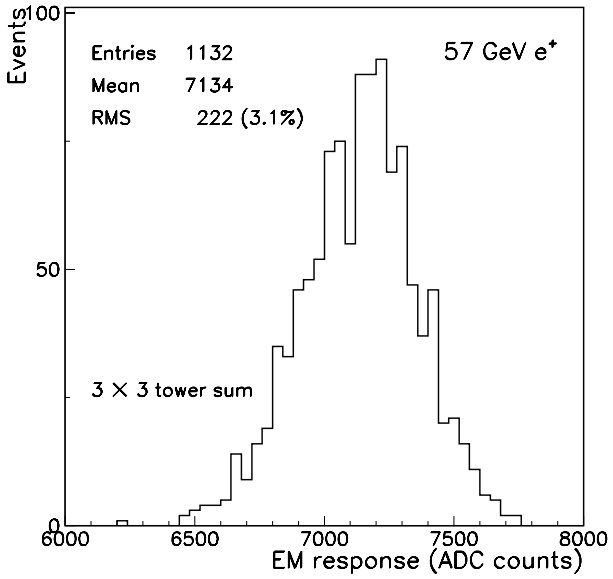

Figure 8: Example of the PEM response to 57 GeV electrons at the reference tower (wedge 1, tower 8), where the response is summed over 3×3 towers.

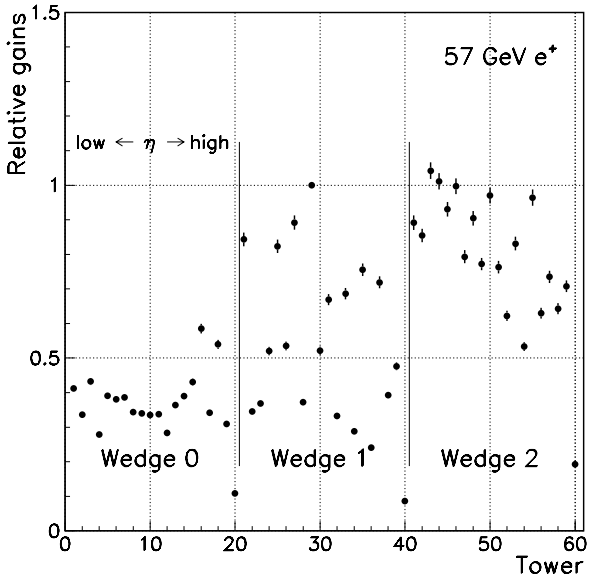

Figure 9: Tile-to-tile response non-uniformity of the PPR.

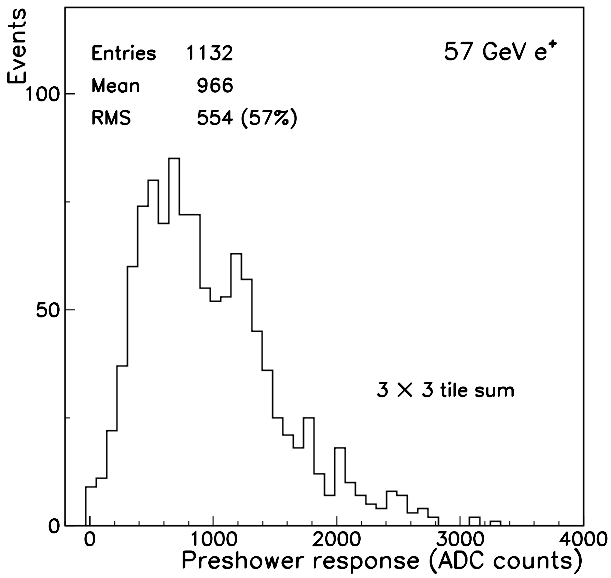

Figure 10: Example of the PPR response to 57 GeV electrons at the reference tower (wedge 1, tower 8), where the response is summed over 3×3 tiles.

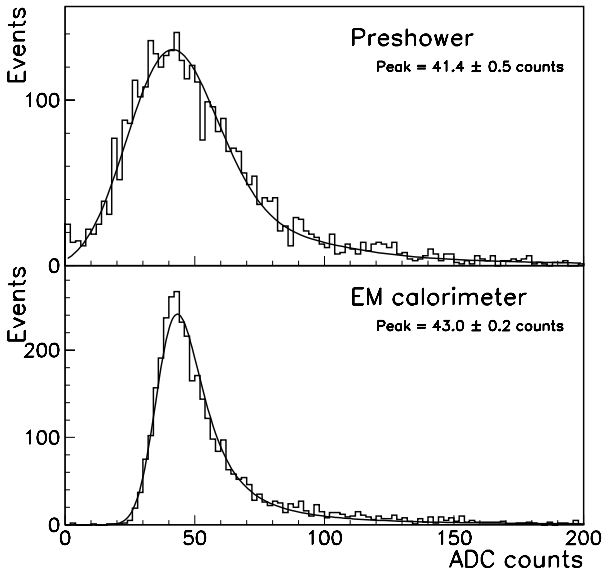

Figure 11: Responses of the PPR and the PEM to 180 GeV muons for the reference tower.

The preshower weight factor is determined by optimizing linearity of the total response as discussed in the next section.

3.4 Linearity

We define the non-linearity for a given energy E by

$$\delta(E) \equiv \frac{\langle E/p \rangle}{\langle E_0/p \rangle} - 1,$$

where E_0 is the normalization energy and we choose the nominal 100 GeV beam. Figure 12 shows the non-linearity at the center of the reference tower as a function of preshower weight w for 11, 28, and 57 GeV electron beams. By taking $w = 0.808$, we can keep the non-linearity less than 1% for both 11 and 28 GeV energies as well as for 57 GeV. The non-linearities with and without adding the PPR response at the center of the reference tower are shown in Fig. 13. Adding the PPR response to PEM response improves the non-linearity at low energies while keeping good linearity at higher energies. The point of this trick is that the weighted sum is only appreciable at low energies because the PPR response is relatively more important with respect to the PEM response.

We could use PES response instead of PPR, since the relative importance of the PES response with respect to the PEM response changes with the incident energy in a qualitatively similar way as the PPR. Figure 14 shows how the non-linearity changes with the PES weight. Note that values of the PES weight has no universal sense because we do not see muon signal-peaks for the PES and do not factor out the phototube gain from the weight values. Non-linearities at various energies in the case of adding PES response have been already shown in Fig. 13. From Fig. 14, we see a larger weight range (shaded area) compared to the PPR case, where both of the non-linearities for 11 and 28 GeV are maintained within $\pm 1\%$. This is because the difference between the PES responses to 11 and 28 GeV electrons is smaller than that for the PPR responses, and weighting is not acting so differently between the two energies. The result indicates that the use of the PES could be more convenient than the PPR in order for a common weight to effectively improve the linearity at low energies. It will be, however, affected more strongly by particle occupancy in the real operation, since the PES is not segmented into a tower geometry. We discuss only the PPR case in what follows.

In the course of *in-situ* calibrations, we could associate for each tower an optimized preshower weight which minimizes the non-linearity of the tower. It seems, however, worthwhile to consider whether the procedure could be simplified; for example, whether the use of a single common weight is effective. The variation of the optimized preshower weights over different towers is induced by the tower-to-tower response non-uniformity which is in principle beam energy dependent. The tower-to-tower response non-uniformity was corrected for 57 GeV electrons, but the same correction is not necessarily effective for other energies. The difference in non-uniformity at various energies is caused by 1) the light-yield non-uniformity over longitudinal layers coupled to the variation of the longitudinal shower shape with energy; 2) the η dependence of the material amount and of the clustering size; and 3) phototube-gain variations during data taking. From 11, 28, and 122 GeV electron data for the eighteen towers W1T02–W1T22, we calculate non-linearities at the low energies with respect to 122 GeV for each tower. By

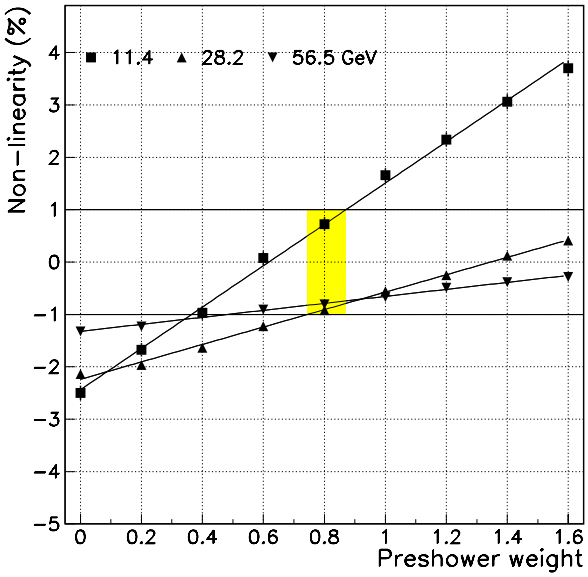

Figure 12: Non-linearities for the beam energies of 11, 28, and 57 GeV as a function of preshower weight at the center of the reference tower.

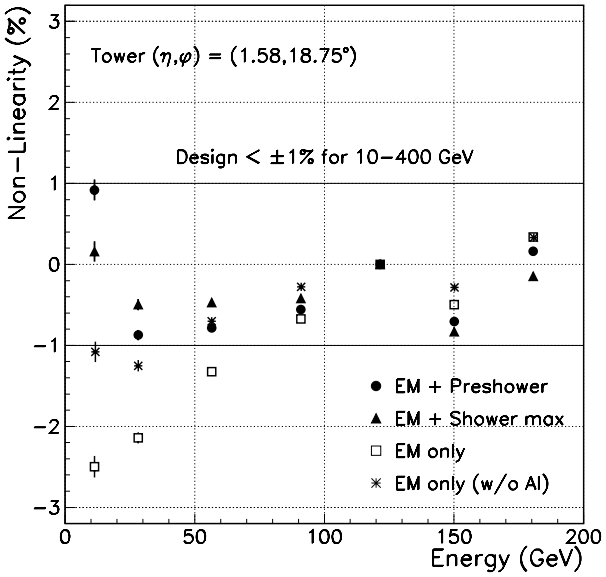

Figure 13: Non-linearities at the center of the reference tower with and without adding the preshower response or the shower-max response. Also, the case without the $0.45X_0$ Al plate is shown for comparison.

Table 3: Energy resolutions at three towers and combined resolution.

Tower	Stochastic term (%)	Constant term (%)
W1T08	14.4 ± 0.2	0.7 ± 0.1
W1T02	15.6 ± 0.2	0.4 ± 0.1
W1T18	14.4 ± 0.2	0.8 ± 0.1
Combined	14.8 ± 0.1	0.8 ± 0.1

looking at the non-linearity distributions over the eighteen towers, the average and rms values (absolute) are found to be +0.2% and 2.3% for the 11 GeV energy, and −0.6% and 1.0% for 28 GeV, respectively. In this study, we correct for the phototube gain variation between the 11 GeV (or 28 GeV) and the 122 GeV (normalization) data taking by using information from the laser calibration system.[5] The design goal is that both the average non-linearity and the rms be smaller than 1% for the energy range of 10–400 GeV, that is, we might expect some towers with non-linearities greater than 1%, while the overall non-linearity (average) and the rms should not be larger than 1%. Only the 11 GeV result fails this goal. Part of the reason could be the η dependence of the non-linearity as shown in Fig. 15. The non-linearity gradually increases along the tower number (larger η), which is seen for both the energies but less for 28 GeV. The trend is qualitatively consistent with better linearities expected at larger η because of less material scaled as $\cos^{-1}\theta$, thus relatively over-weighted preshower responses result in larger non-linearities. It might be necessary to introduce multiple preshower weight factors depending on η to achieve the rms of the non-linearities over towers smaller than 1% for electrons with energy as low as 10 GeV.

Since the average values of the non-linearities over the eighteen towers are within ±1%, we expect the overall non-linearity to be satisfactory. Combining the data for the eighteen towers in which we have similar number of events, we find the non-linearities to be −0.17% and −0.58% for 11 GeV and 28 GeV electrons, respectively.

3.5 Energy resolution

Addition of the preshower response also improves energy resolution.[6] Figure 16 shows the difference in quadrature from the design resolution as a function of preshower weight at the center of the reference tower. Figure 17 shows the energy resolution as a function of beam energy at the center of the reference tower. Fitting to a functional form of $\alpha/\sqrt{E} \oplus \beta$, we obtain $(14.4 \pm 0.2)\%/\sqrt{E} \oplus (0.7 \pm 0.1)\%$, where $\oplus$ represents sum in quadrature. Table 3 lists the measured resolution including two other towers. The result is consistent with the design resolution of $16\%/\sqrt{E} \oplus 1\%$.

Figure 18 shows the resolution of each tower for 57 GeV electrons. For most of the

[5]This correction is accurate to $\simeq 1\%$ which is estimated by looking at the long-term stability of the corrected responses. Thus, the obtained rms values for ratio include a contribution of $\simeq \sqrt{2} = 1.4\%$.

[6]A similar improvement, but to a less extent, is seen when the shower-max response is added instead.

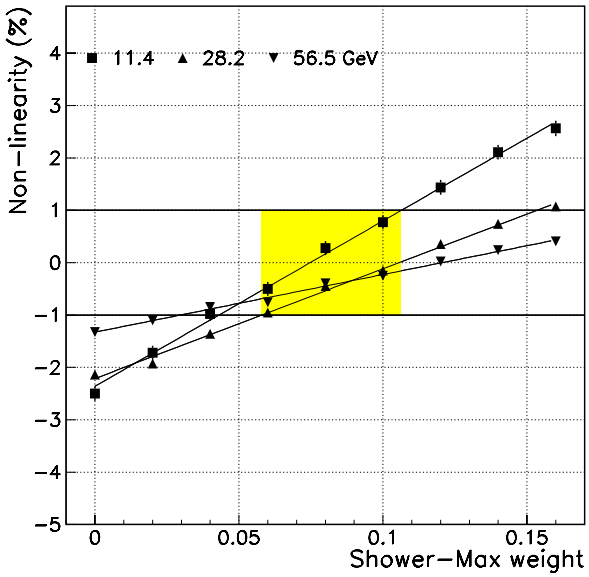

Figure 14: Non-linearities for the beam energies of 11, 28, and 57 GeV as a function of shower-max weight at the center of the reference tower.

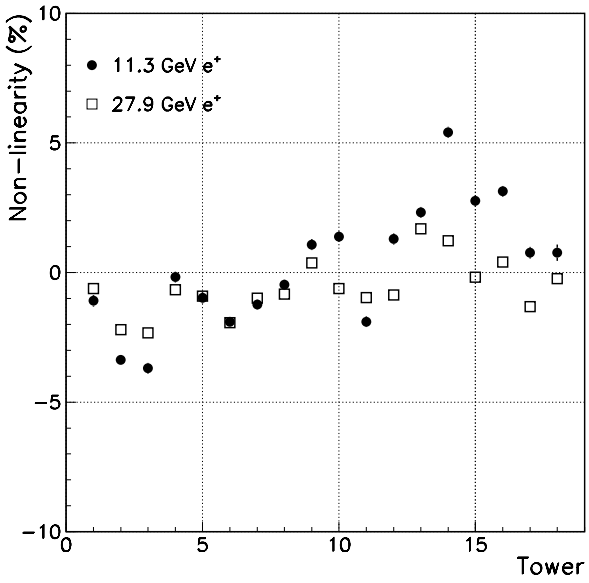

Figure 15: Non-linearity versus tower number. The towers, from left to right in the figure, correspond to W1T02–W1T22.

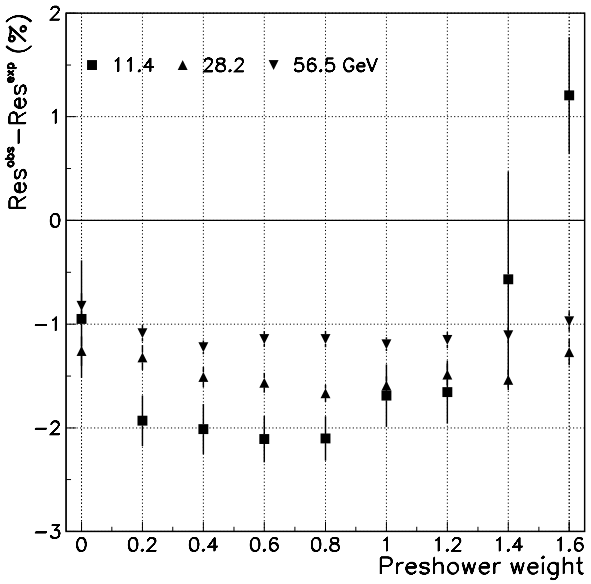

Figure 16: Difference between the measured resolution and the design value as a function of preshower weight at the center of the reference tower.

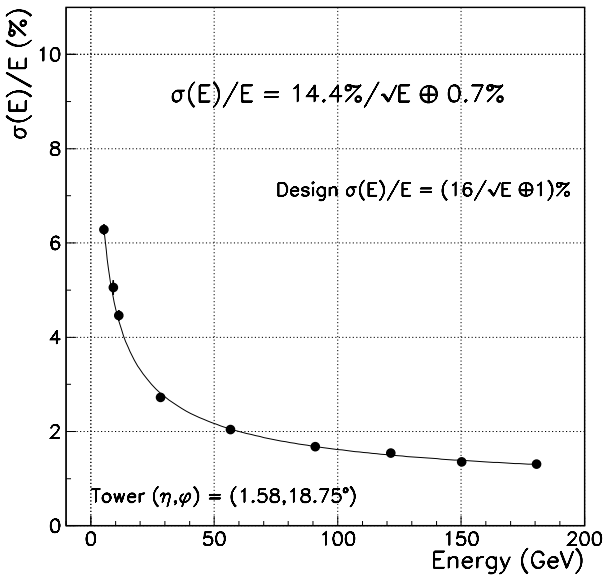

Figure 17: Energy resolution at the center of the reference tower. Preshower response is added to EM response with a weight factor of 0.808.

towers, the resolution is better than 2.4% which is expected from the design resolution for 57 GeV electrons.[7] Combining the data, we obtain the overall resolution to be $(2.51 \pm 0.01)\%$ from 60 towers and $(2.29 \pm 0.01)\%$ omitting towers 0, 1, and 22.

3.6 Transverse response uniformity

We measured the uniformity of the EM response along the tower surface of the reference tower by moving the calorimeter with respect to the 57 GeV electron beam in small steps in η and ϕ. By dividing the tower surface into a mesh of 14×14 cells ($\simeq 0.7$ cm $\times$ 0.7 cm in R and $R\phi$), cell responses are obtained by fitting a Gaussian function to the E/p distribution for each cell. The incident beam position is reconstructed by using the PES. The number of events per cell is over 100 and the statistical uncertainty is usually less than 0.5%. Figure 19 shows the result of the EM response inside and around the reference tower, where the responses are normalized by the average value calculated from all the cells inside the reference tower. Routing of the WLS fiber is schematically shown in Fig. 20. We see higher responses around the fiber position by as much as 5%, while the response drops by $\simeq 6\%$ at the four corners of the tower. The rms of the cell responses inside the tower is 2.1%. This means that there is a $\simeq 2\%$ contribution to the constant term of the EM resolution if we do not apply any corrections for the surface non-uniformity. We obtain similar results for W1T10 and W1T11.

The fine response-map inside towers obtained for the beam test module is effective for the correction of the real detector because the tile-fiber structure is the same. To verify this, we apply the response map obtained for the reference tower to the other two towers (W1T10 and W1T11) as a correction and find the rms of the cell responses inside the towers improved from $\simeq 2.0\%$ to $\simeq 1.5\%$. The residual non-uniformity reflects the fact that the detailed response maps inside towers are not identical among different towers; even for the towers with a similar physical size, as the case we just discussed, due to different optical conditions. We may need to introduce an *in-situ* correction for each tower to eliminate these differences and to further reduce the detector-wide constant term.

3.7 Energy scale

The scale factor C in Eq. (1) is determined by setting $\langle E/p \rangle = 1$. We obtain $C^{-1} = (128.01 \pm 0.08)$ ADC/GeV from the 57 GeV electron data for the center of the reference tower when applying the fine transverse response-map correction. Returning to Eq. (1), the energy scale for the PPR is $128.01 \times 10^{-3}/0.118 = 1.08$ ADC/MeV for the reference tower.

We can estimate the sampling rate for EM showers from the scale factor above. The energy deposited by a MIP in the 22 layers of scintillating tiles is $\simeq 17.6$ MeV, while the muon peak has been found to be 43.0 counts. The conversion between the deposited energy and the ADC counts is thus given by $43.0/17.6 = 2.4$ ADC/MeV. Then, for EM showers, $128/(2.4 \times 10^3) \simeq 5\%$ of the total energy is visible in the scintillators.

[7] The last tower in the figure (W2T22) has a larger value than W0T22 (tower number 20 on the x axis in the figure) with a similar geometry. This is attributed to an overall offset of the beam position by $\simeq 3^\circ$ in ϕ which causes relatively large leakage of showers.

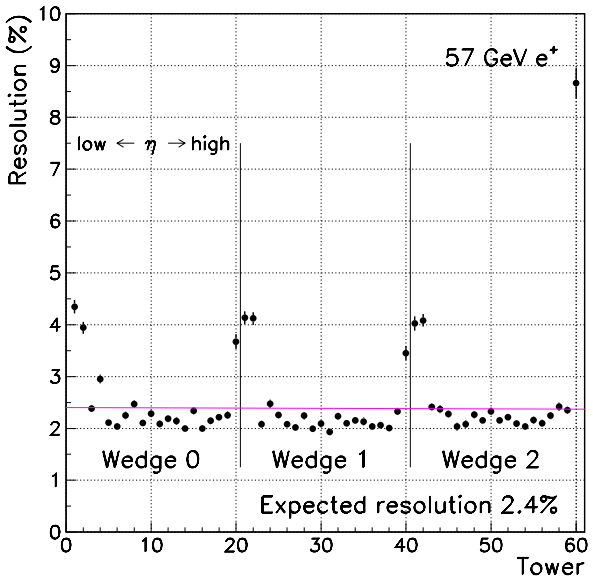

Figure 18: Energy resolution at the center of each tower for 57 GeV electrons.

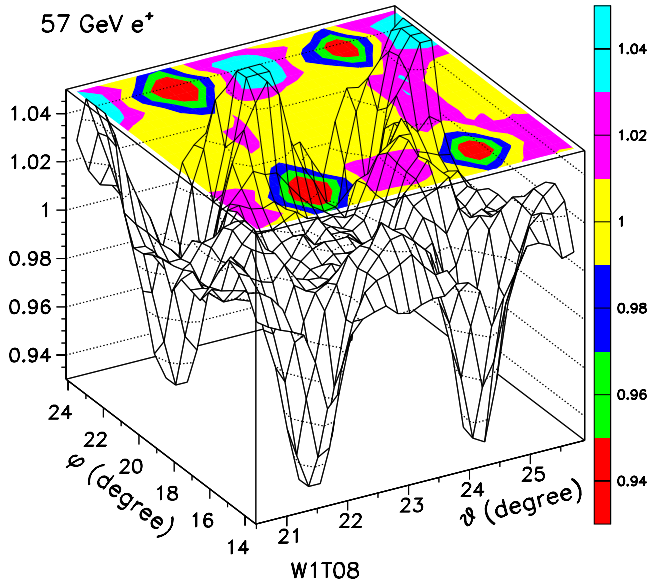

Figure 19: Detailed responses inside and around the reference tower for 57 GeV electrons. They are normalized by the average value of the cell responses inside the tower.

One of the important purposes of this beam test is to find the energy scale of the real detector. This is done by using the wire-source calibration to tie the two detectors. We performed a wire-source calibration a little before the data taking for the energy-scale determination discussed above. The correlation between the results of the wire-sourcing and those of the electron beam limits the accuracy of the transfered energy scale. In Fig. 21, we show the correlation between the two responses by plotting the results for the 48 towers omitting towers 0, 1, 20, and 22. The rms of the ratios is 1.3%. We also check the stability of the correlation in time for the reference tower as shown in Fig. 22. We observe an increase of the response as much as 3% in three months which is due to gain drifts of the phototube known from laser calibration data, while the ratio between the response to electrons and that predicted by the wire-source calibration stays within $\simeq 1\%$. We quote conservatively the accuracy of energy transfer to be $1.3 \oplus 1.0 = 1.6\%$.

It is useful to show the responses of the PPR and the PEM to muons in terms of GeV calibrated with EM showers. They are shown in Fig. 23 for the reference tower. Also, the average PPR response in units of GeV and MIPs as a function of electron energy is shown in Fig. 24 for the reference tower. The number of MIPs is calculated by normalizing the response to that for 180 GeV muons (41.4 counts).

3.8 Energy resolution near the tower boundaries

Energy resolution at various positions inside towers is studied from nine sets of energy-scan data. The average beam-positions are shown in Fig. 25 along with the fine response-map for convenience. The beam spread is $\simeq 1^\circ$ and $\simeq 2^\circ$ in θ and ϕ, respectively. The resolution parameters are shown as open-square points in Fig. 26. Applying a correction by the response map inside and around the reference tower obtained in Section 3.6, the resolution parameters are improved as shown by solid circles in the figure. The combined constant term includes $\simeq 0.7\%$ variation of the average responses from sample to sample, which is a measure of the instability (systematic uncertainty) of the correction. After rescaling responses in each data set, the best resolution for the combined data is $(14.98 \pm 0.07)\%$ and $(0.84 \pm 0.02)\%$ for the stochastic and the constant term, respectively.

By using the constant term for the combined data as a probe, we can infer how fine the transverse response-map should be. The dependence of the constant term on the cell size of the fine response-map is shown in Fig. 27.

3.9 Leakage

Longitudinal EM shower leakage into the hadron calorimeter is studied by looking at the ratio between energies measured by the PEM and the PHA (HAD/EM). We first determine the PHA scale in order to form the ratio on the same scale. As in the PEM case, this is done by setting $\langle E_{\rm tot}/p \rangle = 1$ for pion beams. The total energy $E_{\rm tot}$ is given by $E_{\rm tot} = E_{\rm EM} + C_{\rm HA} E_{\rm HA}$, where the first term, which has been discussed in the previous sections, is in units of GeV, $C_{\rm HA}$ is the scale factor for the PHA in units of GeV/ADC, and $E_{\rm HA}$ is the PHA response in ADC counts. We take a sum over 5×5 towers around the central tower to calculate the PHA response. We use $C_{\rm PHA}^{-1} = (134.9 \pm 1.2)$ ADC/GeV in this leakage study, which is obtained by using the data

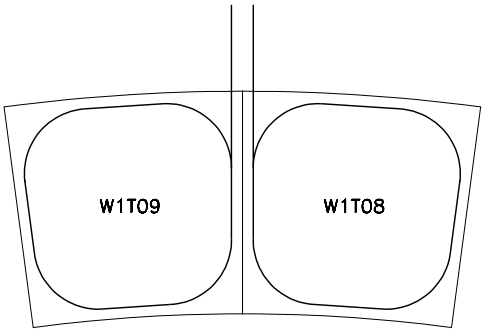

Figure 20: Routing of the WLS fiber in the tile.

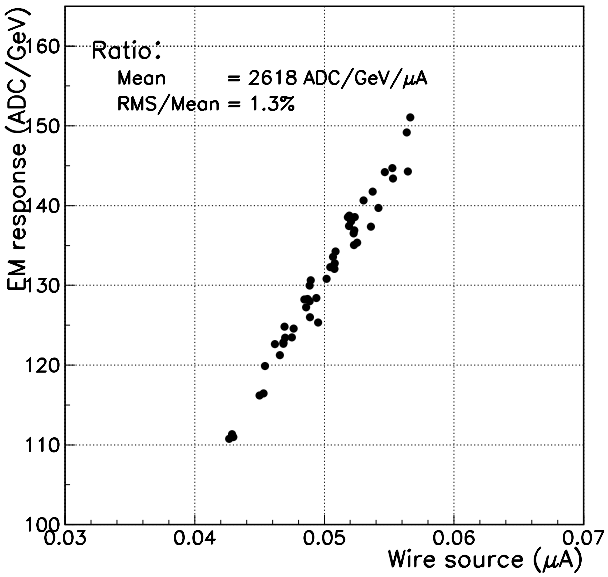

Figure 21: Response to 57 GeV electrons versus response predicted from the wire source calibration.

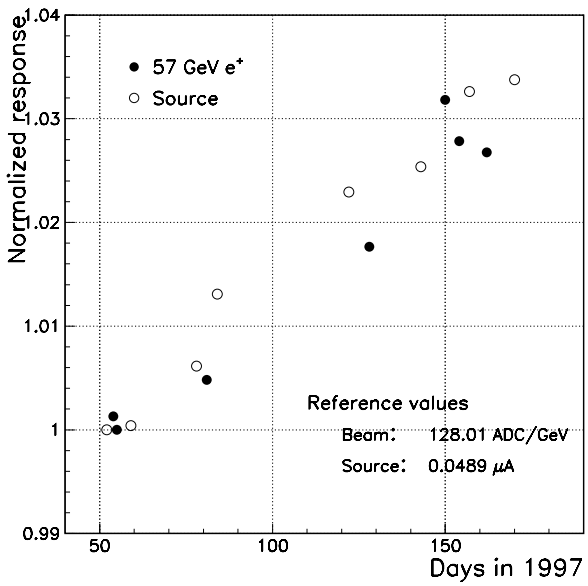

Figure 22: Normalized EM responses to 57 GeV electrons and those predicted by the wire source calibration as a function of day for the reference tower.

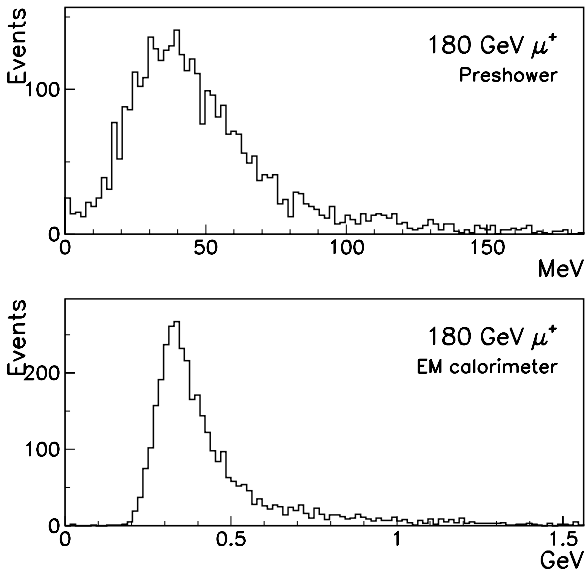

Figure 23: Responses of the PPR and the PEM to 180 GeV muons using the scale determined by electrons for the reference tower.

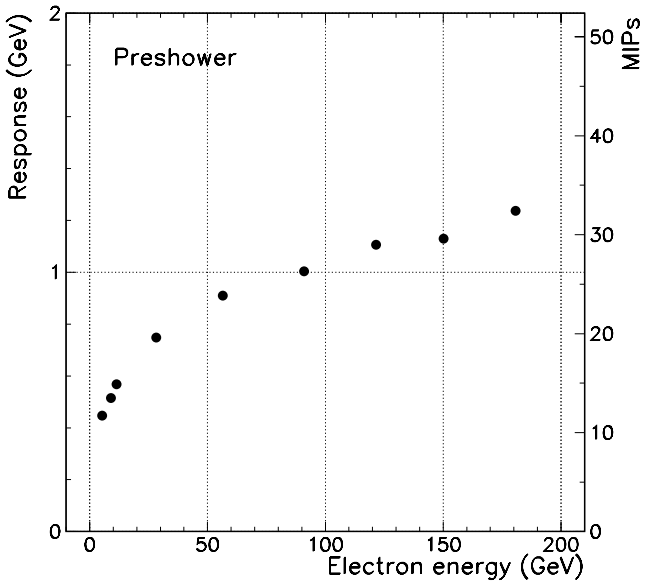

Figure 24: Response of the PPR in units of GeV and MIPs as a function of electron beam energy for the reference tower.

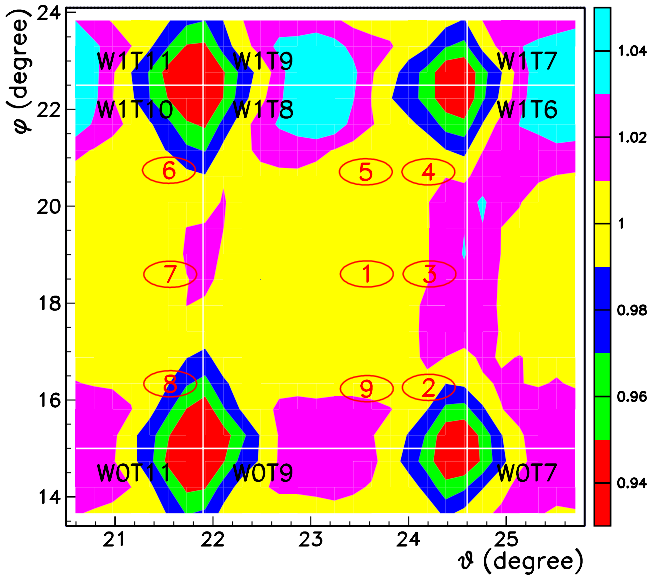

Figure 25: Nine energy-scan data sets to study energy resolution at various positions inside tower. The fine response-map from Fig. 19 is also shown for convenience. Beam spread is $\simeq 1^\circ$ in θ and $\simeq 2^\circ$ in ϕ.

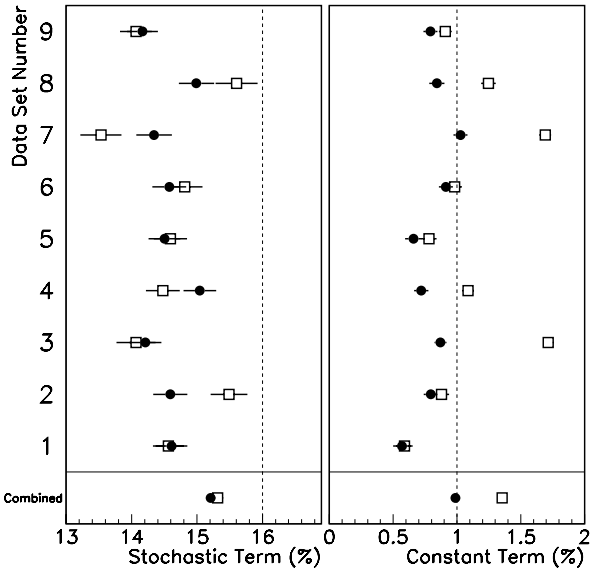

Figure 26: Stochastic and constant terms of the EM resolution at nine different beam positions inside a tower. Open squares show the results without the fine response-map correction and solid circles show the results with correction.

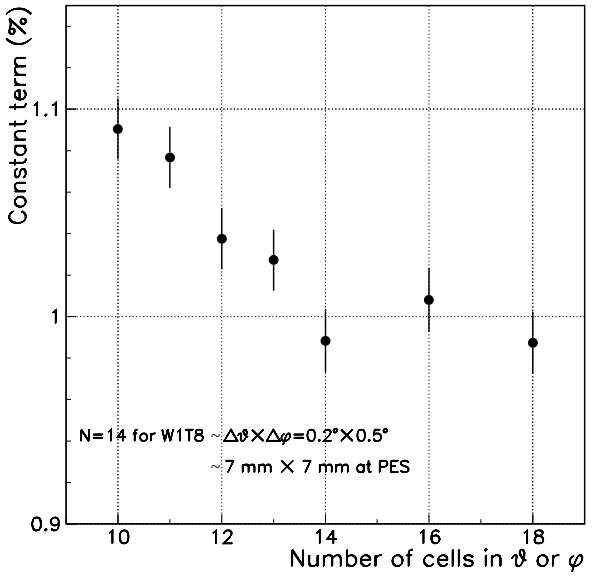

Figure 27: Constant term for the data set combined from those at nine different beam positions as a function of number of cells in θ or ϕ within the reference tower to define the fine response-map. The statistical uncertainties are correlated.

for 58 GeV pions. Figure 28 shows the HAD/EM ratio as a function of electron beam energy.[8] Here, the PHA energy corresponds to the same 3×3 towers as the PEM clustering window. The shaded area represents systematic uncertainties caused by the uncertainty of 1 ADC count in the pedestal subtraction for the PHA responses. The variation of the HAD/EM ratio along the tower number is checked using the data of 57 GeV electrons, and the result is shown in Fig. 29, where towers 0 and 1 are not included since those towers are not covered by the PHA.

We also look at leakage of EM showers in the lateral direction with respect to the beam. The energy ratio between the sum of towers surrounding an inner set of towers and that of the inner towers as a function of beam energy is shown in Fig. 30 for electron data at the center of the reference tower. The beam spread is restricted mainly in the θ direction to be within $\pm 0.45^\circ$ from the tower center.[9] In the figure, "5×5", for example, represents the ratio between the energy sum of 16 towers surrounding the inner 9 towers and the energy measured in the inner 9 towers. The shaded area shows systematic uncertainties originating from pedestal subtraction for the PEM responses for the case of 7×7.[10] The uncertainties for the other cases are almost the same. Dependence on the beam position inside the reference tower is checked for the 5×5 case in Fig. 31 for 57 GeV electrons. The ratio is found to be at most $\simeq 1\%$ around the four corners. Figure 32 shows the energy ratio between the sum over 16 towers surrounding inner 3×3 towers and that for the inner 9 towers for towers 4–13 in wedge 1. This gives the relation between the EM shower containment and the tower size.

3.10 Position resolution

We now discuss information on the beam position provided by calorimetry. One of the possible choices for extracting the beam-position information is to use the energy-weighted average value of tower centers in the clustering window:

$$\boldsymbol{R}_{\rm EM} \equiv \sum_{i}^{3\times 3} \boldsymbol{R}_i \frac{E_i}{E},$$

where $\boldsymbol{R}_i$ is the 2-dimensional vector in the R-ϕ plane pointing to the center of the ith tower. We present only the results for $R_{\rm EM} = |\boldsymbol{R}_{\rm EM}|$ in detail because similar results are obtained for $R_C\phi$, where R_C is R of the tower center.

How the $R_{\rm EM}$ traces the beam position reconstructed by tracking information ($R_{\rm TRK}$) is shown in Fig. 33, together with the fluctuation of the $R_{\rm EM}$. Simply taking the $R_{\rm EM}$ as an estimator for $R_{\rm TRK}$, the resulting R resolution is a few cm in terms of the rms. If we consider Fig. 33 as a "map" to convert $R_{\rm EM}$ to estimate $R_{\rm TRK}$, the corresponding resolution in terms of the rms is shown in Fig. 34 as a function of corrected $R_{\rm EM}$.

Another possible quantity related to R is the response asymmetry between the towers in

[8] In a strict sense, the HAD/EM introduced here is closer to the leakage fraction out of the total induced energy because the PEM scale has been already calibrated by using electron beam momentum.

[9] It corresponds to about the lower half of the beam-position distribution in the x direction shown in Fig. 5.

[10] The 7×7 window is actually partial but includes the largest number of towers, thus the most conservative case for the uncertainty estimation.

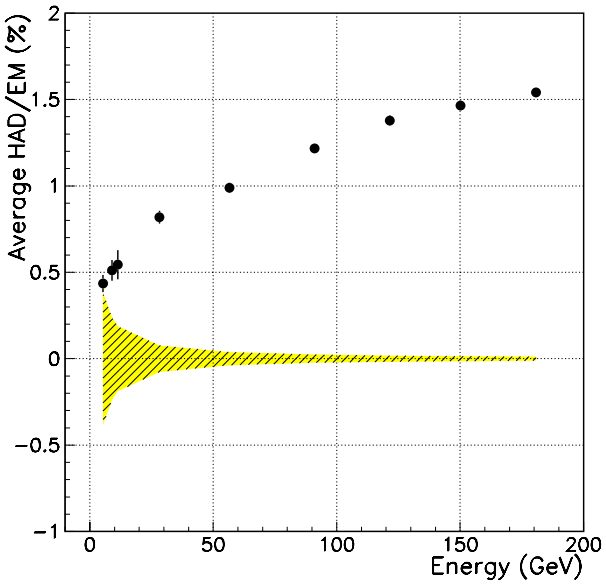

Figure 28: Ratio between the PEM and PHA responses as a function of electron beam energy. The shaded area represents systematic uncertainties originating from pedestal subtraction.

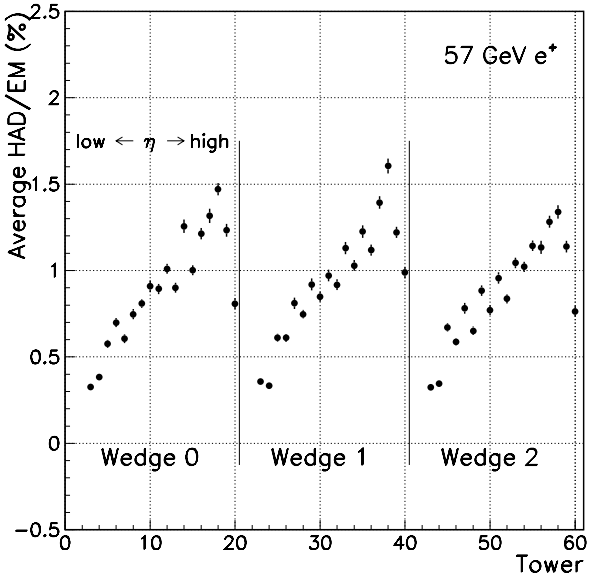

Figure 29: Ratio between the PEM and PHA responses for each tower. The first two towers in each wedge are not included because there are no corresponding PHA towers.

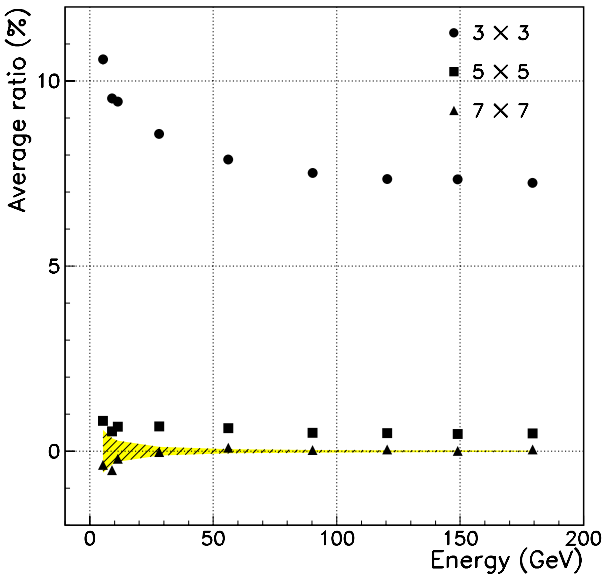

Figure 30: Ratio between the energy sum over surrounding towers and that over inner towers as a function of electron beam energy. Electrons are required to hit a central region of the reference tower. The shaded area represents systematic uncertainties originating from pedestal subtraction.

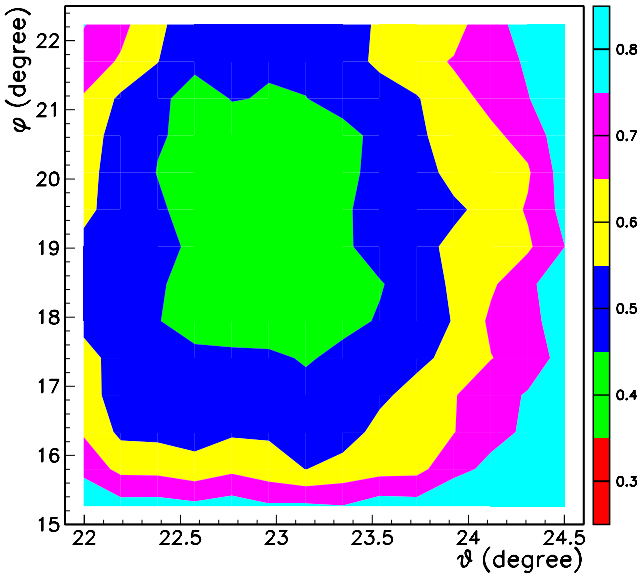

Figure 31: Ratio between the energy sum over 16 towers surrounding inner 3×3 towers and the energy in the inner 9 towers, given along the surface of the reference tower for 57 GeV electrons. The ratio is in units of percent.

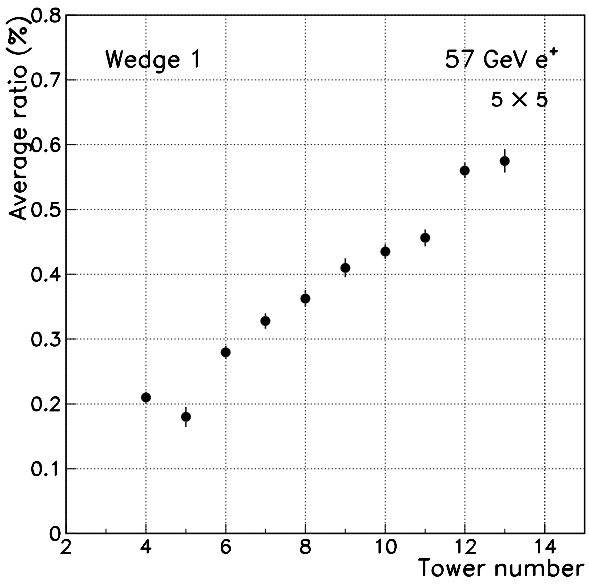

Figure 32: Ratios between the energy sum over towers surrounding the 3×3 window and that in the inner 9 towers shown for several towers in wedge 1.

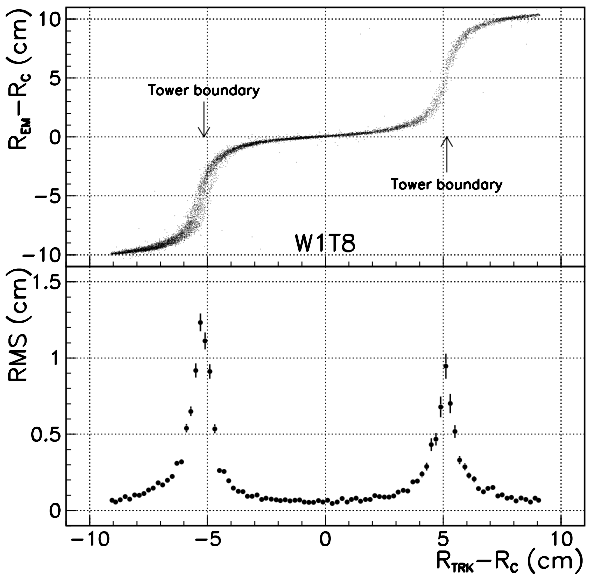

Figure 33: Relation between the energy-weighted R given by calorimetry and the R given by tracking around the reference tower.

the upper and lower side of the central tower:

$$A_{\rm UD} \equiv \frac{E_{\rm up} - E_{\rm down}}{E_{\rm up} + E_{\rm down}}.$$

The relation between the $A_{\rm UD}$ and $R_{\rm TRK}$ is given in Fig. 35. In the lower plot is shown the resolution that we would have after applying the map given in the upper plot.

Resolutions for the energy-weighting method at various towers are given in Fig. 36. In this, the estimated R or $R_C\phi$ are restricted within ± 1 mm around the center of each central tower in the clustering window, which corresponds to choosing the region where the resolution is the poorest (see Fig. 34). Also, the data for three towers with the same tower number in the three wedges are combined to gain statistics. Finally, towers 0 and 1 (1 and 2 on the x axis in the figure) are not included because the beam position is far off the tower center. As a result of less sampling at towers 0 and 1, there are larger fluctuations, and thus the R resolutions at towers 1 and 2 are expected to be worse than others. Except for this, the R resolution is almost flat over all the towers because the tower segmentation in the R direction does not change much. On the other hand, the ϕ resolution becomes better toward higher η due to finer segmentation in the length scale. The energy dependence of the R resolution around the tower centers is shown in Fig. 37 for three towers at different η's.

3.11 Lateral shower profile

In electron identification, a significant fraction of charged hadrons are rejected by requiring a large energy deposition in the EM section compared to that in the hadronic section. For example, only $< 1\%$ of pions survive a cut, HAD/EM < 0.1, in the energy range above 50 GeV as shown in Fig. 38.[11] The efficiencies for electrons are $> 99\%$ for this cut. The lateral shower profile would also help to reduce residual pions depositing a large fraction of energy in the EM section.

We introduce a χ^2-like parameter to quantify the lateral shower profile:

$$\chi^2_{3\times 3} = \frac{1}{N_{\rm tower}} \sum_i^{3\times 3} \left(\frac{E_i/p - \overline{E_i/p}}{\sigma_{E_i/p}} \right)^2 ,$$

where $\overline{E_i/p}$ and $\sigma_{E_i/p}$ are respectively the average and rms of the E/p ratio for the ith tower in the clustering window, obtained by using electron beam data. The average $\chi^2_{3\times 3}$ is $\simeq 1$ for electrons. The parameterization for the signal, namely $\overline{E_i/p}$ and $\sigma_{E_i/p}$, is expected to depend on the position of beam incidence within the central tower in the clustering window, the tower size, and the beam energy. We use the fine position-scanning data of 57 GeV electrons discussed in Section 3.6 to divide the reference tower into 14×14 cells and obtain a parameterization for each cell. By knowing which cell is hit by a beam particle using the PES, the corresponding $\overline{E_i/p}$ and $\sigma_{E_i/p}$ are used in the calculation of $\chi^2_{3\times 3}$. In Fig. 39, we compare the $\chi^2_{3\times 3}$ distributions for the same electron data and for 58 GeV pions, where the pions are required to satisfy HAD/EM < 0.1 and $0.7 < E_{\rm EM}/p < 1.3$. If we impose a cut of $\chi^2_{3\times 3} < 5$, for example, $\simeq 99\%$ of electrons survive

[11] In the figure, the statistical uncertainties differ from point to point somewhat randomly. Since the HAD/EM < 0.1 cut rejects pions so much, we have to combine as many data samples as possible, which results in rather non-uniform statistical sizes.

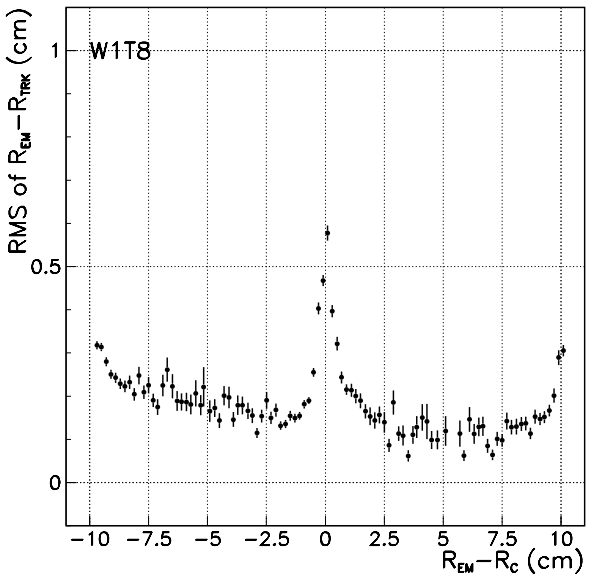

Figure 34: Resolution of R after correcting raw $R_{\rm EM}$ with a map between $R_{\rm EM}$ and $R_{\rm TRK}$.

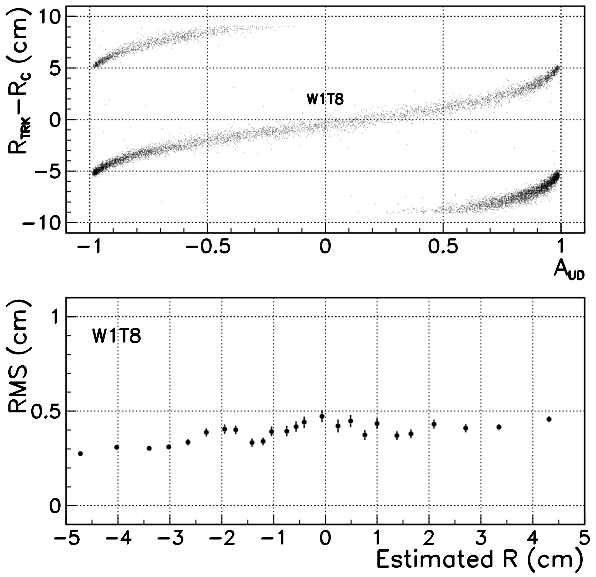

Figure 35: Upper) Relation between the asymmetry parameter $A_{\rm UD}$ and the beam position. Lower) The rms of differences between $R_{\rm TRK}$ and the R estimated from a value of $A_{\rm UD}$.

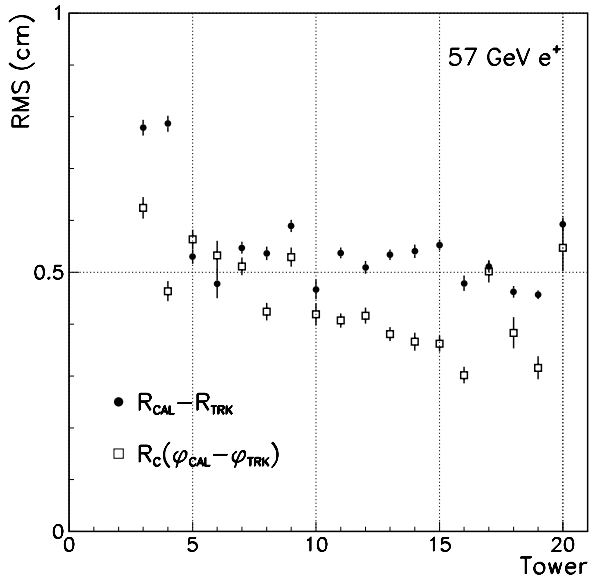

Figure 36: Resolutions of R and $R_C\phi$ around the centers of various towers. The R and $R_C\phi$ are estimated from an energy-weighted sum of tower centers in clustering windows.

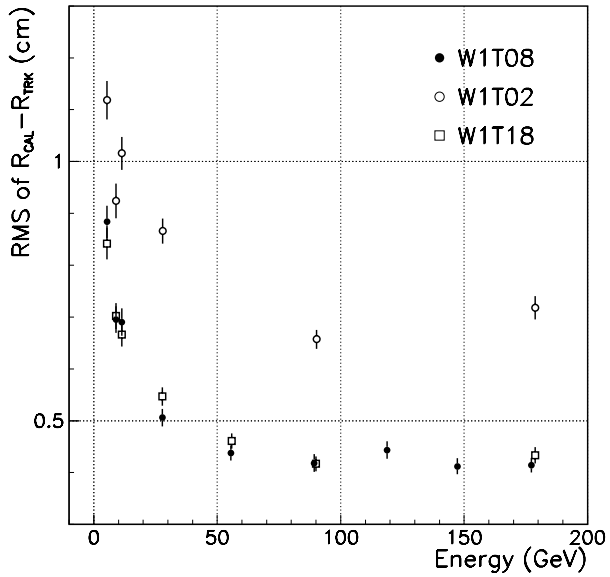

Figure 37: Resolutions of R around the centers of three different towers as a function of electron beam energy. The R is estimated from an energy-weighted sum of tower centers in clustering windows.

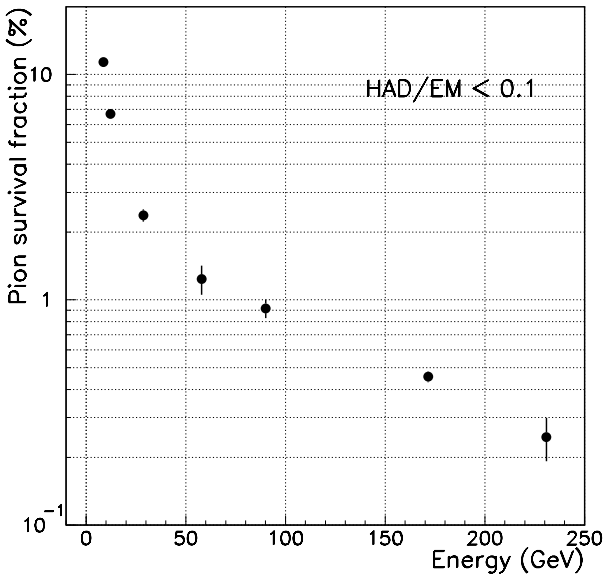

Figure 38: Fraction of pions surviving the HAD/EM < 0.1 cut for various energies.

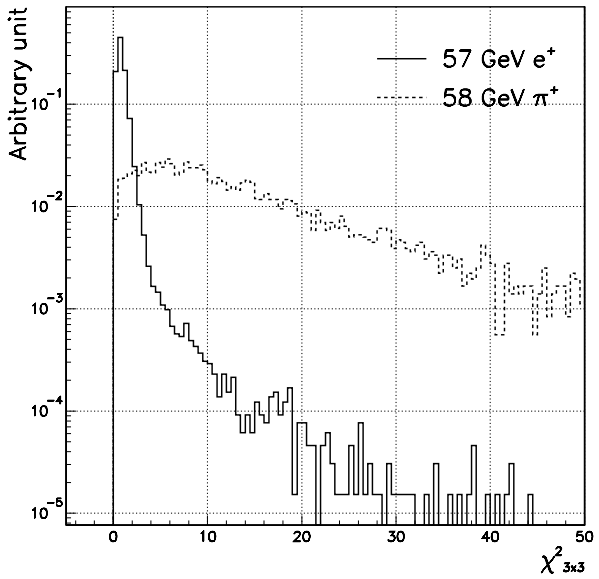

Figure 39: Distributions of $\chi^2_{3\times3}$ for 57 GeV electrons and 58 GeV pions. The pions are required to satisfy HAD/EM < 0.1 and $0.7 < E_{\rm EM}/p < 1.3$.

the cut while only $\simeq 20\%$ of pions do. The separation power originates from the fact that pions have larger lateral spread and larger fluctuations compared to EM showers.

We check the energy dependence of the e-π separation. The parameterization is obtained for each energy by using electron energy-scan data. The efficiency for pions as a function of beam energy is shown in Fig. 40. We see less separation powers at low and high energies. The former is because the larger shower fluctuation for electrons diminishes the separation power, while the latter is because the shower shape of the EM part for pions gets more biased by the selection cuts and becomes similar to that for electrons.

We expect less separation power if we take a set of parameterizations based on coarser meshes. We check this point by changing the number of cells, and the result is shown in Fig. 41.

3.12 Effects of material present

We took a set of energy-scan data without the Al plate in front of the calorimeter. The non-linearity for this case is included in Fig. 13. As expected, the linearity is better at low energies with less material. We do not see much difference in the resolution. It is $(14.7 \pm 0.2)\%/\sqrt{E} \oplus (0.6 \pm 0.1)\%$ with an optimized preshower weight of 0.589. There is less than 1% difference in the energy scale. The HAD/EM ratio and the lateral leakage are found to be unchanged, but with slight shifts ($\simeq 0.3\%$), especially at high energies, upward for the HAD/EM ratio and downward for the lateral leakage.

The actual amount of the material in the operation in CDF is not known precisely. We expect contributions of about $0.53X_0$ from silicon detectors, $0.28X_0$ from the endplate of the central tracking detector, and an additional amount from cables, connectors, etc. of which the total is uncertain. A study showed that, in the previous collider runs at CDF, there was as much as $0.35X_0$ of material which could be attributed to miscellaneous components [17]. The depths of the preshower detector and the shower-max detector in Table 1 are given using this number.

4 Conclusions

We tested a module which was a 45°-ϕ section of the CDF Plug Upgrade calorimeter at the Fermilab Meson-Test beamline. The energy resolution of the EM calorimeter to the positron beam is consistent with the expectation of $16\%/\sqrt{E} \oplus 1\%$ with a trend of being better at the centers of the towers: $14\%/\sqrt{E} \oplus 0.7\%$ at a typical tower. It was shown that the addition of the preshower response to the EM calorimeter response with an optimized weight reduced the non-linearity to only 1% for positrons with energies in the range of 11–181 GeV. It seems, however, that the use of a single common weight cannot linearize the response of all towers in the detector to better than 1%. We obtained a detailed transverse response map inside a tower with 57 GeV positrons and found the response non-uniformity over the surface of the tower to be about 2%. From a study applying the map to other towers, we expect the map to reduce the response non-uniformity over the surface to about 1.5% for towers of the real calorimeter, reflecting the similarity of the tile-fiber structure among the towers. The map was also found to

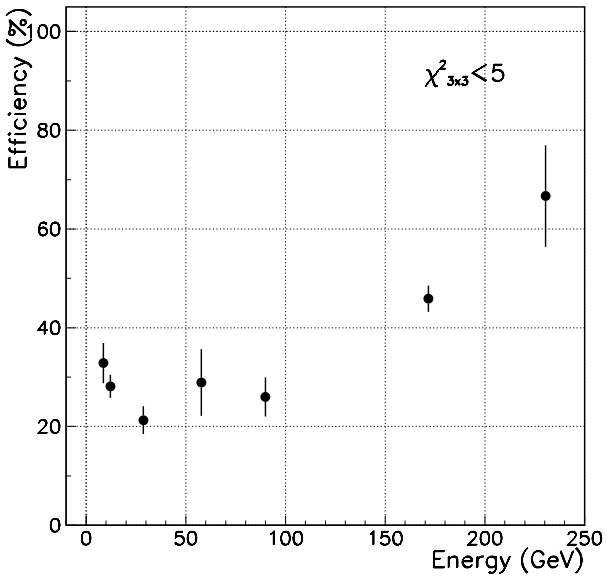

Figure 40: Efficiency of the $\chi^2_{3\times3} < 5$ cut for various energies of pions. The pions are required to satisfy HAD/EM < 0.1 and $0.7 < E_{\rm EM}/p < 1.3$.

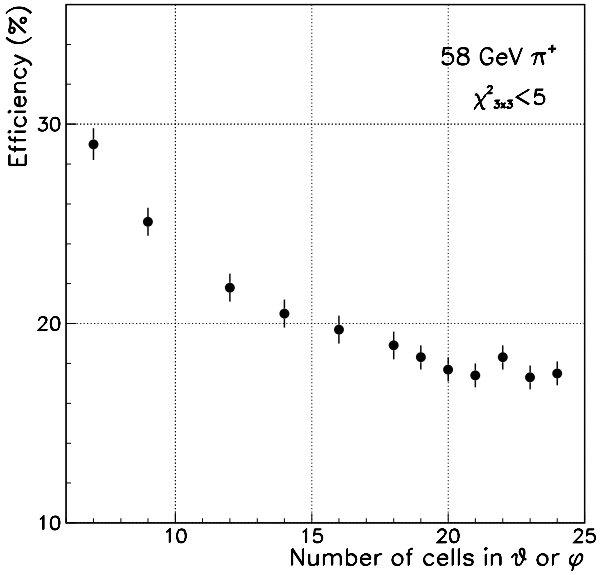

Figure 41: Efficiency of the $\chi^2_{3\times3} < 5$ cut for 58 GeV pions as a function of number of cells in θ or ϕ within the reference tower to define parameterizations for the $\chi^2_{3\times3}$ calculation. The pions are required to satisfy HAD/EM < 0.1 and $0.7 < E_{\rm EM}/p < 1.3$. The statistical uncertainties are correlated.

be effective in reducing the constant term of the energy resolution at positions near the tower boundaries. The longitudinal EM shower leakage in terms of the energy ratio between the EM and hadronic calorimeter is 0.5–1.5% depending on the positron energy from 5 GeV to 181 GeV, and is also found to vary as 0.3%–1.6% from low η to high η towers. The EM shower leakage into towers surrounding the cluster of 3×3 towers used in measuring the energy is 0.2–1%, depending on the positron energy, η, and beam position inside the tower. The position resolution using the calorimeter towers was found to be about 5 mm for 57 GeV positrons degrading to about 1 cm at 5 GeV. The lateral shower profile helps distinguish positrons from charged pions that deposited a large fraction of their energies and would mimic electron signatures. By forming a χ^2-like parameter from the array of 3×3 tower responses divided by the beam momentum, and requiring the value, for example, to be less than 5, 58 GeV pions are reduced by a factor of 5 while being almost fully efficient for positrons. The wire-source calibration, as a means to transfer the energy scale determined for the beam test module to the real detector, was successfully done with an accuracy of 1–2%.

Acknowledgements

We would like to thank A. Bassi and M. Deninno of University of Bologna for their contributions. We also thank the Fermilab staff and the technical staffs of the participating institutions for their vital contributions. This work was supported by the U.S. Department of Energy and National Science Foundation; the Italian Istituto Nazionale di Fisica Nucleare; and the Ministry of Education, Science, Sports and Culture of Japan.

References

[1] G. Apollinari, P. de Barbaro, and M. Mishina, in: A. Menzione *et al.* (Eds.), Proceedings of the Fourth International Conference on Calorimetry in High Energy Physics, La Biodola, Italy, 1993, World Scientific, Singapore, 1994, p. 200.

[2] R. Blair *et al.*, CDF Collaboration, CDF II Technical Design Report, FERMILAB-Pub-96/390-E, 1996, p. 9-1.

[3] V. Kryshkin and A. Ronzhin, Nucl. Instr. and Meth. A 247 (1986) 583.

[4] M. Albrow *et al.*, Nucl. Instr. and Meth. A 256 (1987) 23.

[5] L. Balka *et al.*, Nucl. Instr. and Meth. A 267 (1988) 272.

[6] S. Bertolucci *et al.*, Nucl. Instr. and Meth. A 267 (1988) 301.

[7] F. Abe *et al.*, Nucl. Instr. and Meth. A 271 (1988) 387.

[8] T. Asakawa *et al.*, Nucl. Instr. and Meth. A 340 (1994) 458.

[9] S. Aota *et al.*, Nucl. Instr. and Meth. A 352 (1995) 557.

[10] S.H. Kim, CDF Collaboration, Nucl. Instr. and Meth. A 360 (1995) 206.

[11] S. Aota *et al.*, Nucl. Instr. and Meth. A 420 (1999) 48.

[12] T. Asakawa *et al.*, Nucl. Instr. and Meth. A 452 (2000) 67.

[13] K. Hara *et al.*, Nucl. Instr. and Meth. A 348 (1994) 139.

[14] S. Aota *et al.*, Nucl. Instr. and Meth. A 357 (1995) 71.

[15] G. Apollinari *et al.*, Nucl. Instr. and Meth. A 412 (1998) 515.

[16] M. Albrow *et al.*, Nucl. Instr. and Meth. A 431 (1999) 104.

[17] T. Ino, Ph.D. thesis, University of Tsukuba, 1996.

[18] G. Drake *et al.*, Nucl. Instr. and Meth. A 269 (1988) 68.

[19] V. Barnes, A. Laasanen, and J. Ross, in: H. Gordon and D. Rueger (Eds.), Proceedings of the Second International Conference on Calorimetry in High Energy Physics, World Scientific, Singapore, 1994, p. 338.

[20] V. Barnes, A. Laasanen, A. Pompos, and M. Wilson, in: A.D. Bross, R.C. Ruchti, and M.R. Wayne (Eds.), Proceedings of SCIFI 97: Workshop on Scintillating Fiber Detectors, Notre Dame, IN, USA, 1998, p. 420.

[21] D. Cauz *et al.*, in: D.F. Anderson *et al.* (Eds.), Proceedings of the Sixth International Conference on Calorimetry in High Energy Physics, Frascati, Italy, Frascati Physics Series, 1996, p. 369.